



Article

# Optimization Design of Variable Reluctance Resolver Based on Three-phase Symmetrical Winding

Xinmin Li <sup>1</sup> , Jiannan Chen <sup>1</sup> and Zhen Zhang <sup>2,\*</sup>

<sup>1</sup> School of Electrical Engineering, Tiangong University, Tianjin 300387, China; lixinmin@tju.edu.cn (X.L.); 2131070892@tiangong.edu.cn (J.C.)

<sup>2</sup> Advanced Electrical Equipment Innovation Center, Zhejiang University, Hangzhou 311107, China

\* Correspondence: zzhen@zju.edu.cn

**Abstract:** In order to ease the structure and manufacturing process of the variable reluctance (VR) resolver, the three-phase symmetrical single-layer winding commonly used in the stator winding of permanent magnet synchronous motors (PMSM) is applied to the VR resolver in this paper. The proposed resolver has the same winding direction and number of turns on all teeth. And the non-overlapping distribution of the three-phase windings of the resolver is ensured. For this novel resolver, the resolver-to-digital conversion (RDC) method references the ultra-high-frequency (UHF) signal injection method used when a PMSM is powered off and restarted. Instead of the need for the orthogonal envelope RDC required by conventional resolvers, the absolute position of the rotor can be obtained. In this paper, the prototype of the proposed resolver and the peripheral circuits are fabricated and compared with the position detected by the optical encoder, and the validity of the proposed resolver and the accuracy of the RDC are verified by the results of the comparison experiments.

**Keywords:** optimization design; resolver-to-digital conversion; single-layer winding; symmetrical winding; ultra-high frequency signal injection; variable reluctance resolver



**Citation:** Li, X.; Chen, J.; Zhang, Z. Optimization Design of Variable Reluctance Resolver Based on Three-phase Symmetrical Winding. *World Electr. Veh. J.* **2024**, *15*, 201. <https://doi.org/10.3390/wevj15050201>

Academic Editor: Peter Van den Bossche

Received: 8 April 2024

Revised: 1 May 2024

Accepted: 4 May 2024

Published: 6 May 2024



**Copyright:** © 2024 by the authors. Licensee MDPI, Basel, Switzerland. This article is an open access article distributed under the terms and conditions of the Creative Commons Attribution (CC BY) license (<https://creativecommons.org/licenses/by/4.0/>).

## 1. Introduction

In the permanent magnet synchronous motor (PMSM) drive system, whether an accurate and real-time rotor position can be obtained directly affects the control performance [1–4]. Position sensors for permanent magnet synchronous motors include Hall sensors, optical encoders, and resolvers [5–7]. Hall sensors have a small, inexpensive, and simple structure, but the position detection resolution is low. The optical encoder position detection accuracy is high, but the poor adaptability to harsh environments and the cost are also high. Resolver has the advantages of a simple structure, being easy to install, shock resistance, adaptability to harsh environments, and a wide range of rotational speeds, so resolver in the permanent magnet synchronous motor is more widely applied [8–11]. The resolver is mainly divided into a brushless and a variable-reluctance (VR) resolver [12]. Although the accuracy of the brushless resolver is higher than that of the VR resolver, the VR resolver has higher mechanical strength and a simpler structure because its rotor has no winding, and all windings are wound on the stator [13–15]. However, the way of winding the stator winding and the flexibility of pole-slot coordination in the VR resolver are still diverse. Many scholars have conducted extensive research on further simplifying the structure of the VR resolver.

The stator winding forms of conventional VR resolvers are concentrated equal-turn winding and sinusoidal distributed winding, respectively. The excitation winding of the concentrated equal-turn winding is wound in a back-to-back manner, while the sine and cosine output windings are wound in a back-to-back manner with a gap between teeth. The number of turns per tooth of the sine and cosine output windings is the same,

but this winding method is limited by the fact that the number of stator teeth is four times the number of pole pairs. The requirement for smaller installation dimensions in specific situations limits the application of this structure [16]. The sinusoidal distribution winding structure breaks the limitation of the rotor pole pair number of the resolver by the number of stator teeth, and its excitation winding still adopts the back-to-back winding method. However, the sine and cosine output windings use the number of turns per tooth to vary according to the sine function, which improves the flexibility of pole-slot coordination. However, the number of turns of the output winding under each tooth is different, which greatly increases the complexity of the manufacturing process [17,18]. In addition, centralized equal-turn windings have two sets of windings under each tooth, and sinusoidally distributed windings have three sets under each tooth, which significantly increases the risk of short-circuit failures in the windings of the resolver [19].

Ge X et al. proposed a new type of resolver with a non-overlapping winding structure. That is, there is only one set of windings under each stator tooth, and this structure is considered to be the simplest structure of the VR resolver. However, the winding structure proposed by them is only applicable to resolvers with special pole-slot coordination. Taking the 12-tooth stator as an example, it is only applicable to VR resolvers with pole pairs of 1, 5, and 7 [8,20]. In motor drive systems, permanent magnet synchronous motors often use resolvers with the same number of pole pairs as the motor to ensure that the calculated electrical angle remains consistent. This structure limits the application of resolvers in certain situations [21]. To solve the limitation in flexibility in the coordination of non-overlapping winding pole-slots, Saneie H. et al. proposed a unique winding method. However, this method still increases the complexity of the manufacturing process of the VR resolver, particularly in terms of the complexity of winding and the unequal number of turns [22].

To ease the structure and manufacturing process of VR resolvers, numerous studies have been conducted in various publications. However, existing research has primarily targeted the generation of orthogonal signals from the VR resolver, with no paper discussing the special case where the output signals from the VR resolver are non-orthogonal [23]. In this paper, a new type of VR resolver with three symmetrical windings is proposed, in which the three symmetrical single-layer winding structures of PMSM are applied to the resolver so that the winding direction, as well as the number of turns under all stator teeth of the resolver, are the same and the form of the winding distribution is a non-overlapping distribution. The resolver-to-digital conversion (RDC) method of this novel resolver draws reference to the ultra-high frequency (UHF) injection method employed by Internal permanent magnet synchronous motors (IPMSM) during power-off and restarted conditions, enabling the calculation of the absolute rotor position of the resolver without utilizing conventional orthogonal RDC methods [24–26]. The proposed VR resolver is mainly used in PMSM drive systems for electric vehicles, which can simplify the structure and manufacturing process of the conventional VR resolver in order to speed up the production cycle of the resolver.

This paper first analyzes the operational principles of the traditional orthogonal VR resolver. Secondly, an optimized design method for the VR resolver with three-phase symmetric windings has been proposed, and theoretical derivation has been conducted. The final experimentation was conducted using the corresponding RDC method and peripheral circuits, validating the feasibility of the proposed resolver.

## 2. Operation Principle of a Conventional Orthogonal VR Resolver

The structure of the VR resolver is illustrated in Figure 1. Given that the rotor of the VR resolver does not possess windings, the stator is equipped with three sets of windings, namely the excitation windings R1R2, the sine output windings S2S4, and the cosine output windings S1S3.

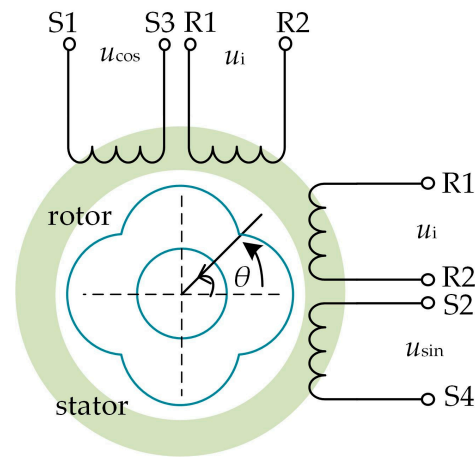


**Figure 1.** Structure of a conventional VR (variable reluctance) resolver.

The magnetic permeability of the  $i$ th stator tooth of the VR resolver can be expressed as follows:

$$\Lambda_i = \Lambda_0 + \sum_{\mu=1}^{\infty} \Lambda_{\mu} \cos[\mu P\theta + (i - 1) \frac{2\mu P\pi}{Z_s}] \quad (1)$$

The sum of the magnetic permeabilities under all stator teeth can be expressed as follows:

$$\sum_{i=1}^{Z_s} \Lambda_i = Z_s \Lambda_0 + \sum_{\mu=1}^{\infty} \sum_1^{Z_s} \Lambda_{\mu} \cos[\mu P\theta + (i - 1) \frac{2\mu P\pi}{Z_s}] \quad (2)$$

This is because the excitation winding is wound on each stator tooth with an equal number of turns. Ignoring higher-order harmonics, the self-inductance of the excitation winding,  $L_1 = N^2 Z_s \Lambda_0$ , is constant. The input reaction can be expressed as follows:

$$X = \sum_{i=1}^{Z_s} \omega N^2 \Lambda_i = j2\pi f N^2 \cdot Z_s \Lambda_0 \quad (3)$$

Therefore, when excited with a constant Alternating Current voltage, its excitation current is also constant.

Since the sine-cosine output windings are spatially distributed with a 90-degree difference in electrical angle and are spaced apart and counter-wound, the mutual inductance coefficients  $M_s$  and  $M_c$  vary with the rotation of the rotor at an electrical angular velocity  $\omega_e$ , i.e.,  $M_s = M_m \sin(\omega_e t)$  and  $M_c = M_m \cos(\omega_e t)$ , where  $M_m$  is the magnitude of the mutual inductance. The equivalent winding model of the conventional VR resolver is depicted in Figure 2.

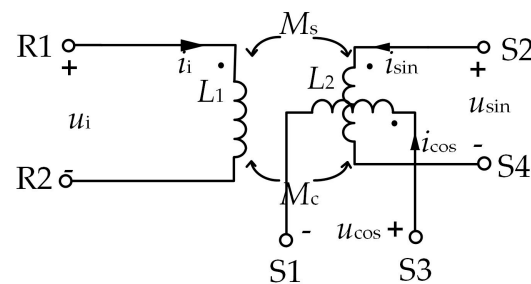


**Figure 2.** Equivalent winding model of the conventional VR resolver.

During the operation of the resolver, the sine and cosine output windings are approximately open-circuited. When excited by a high-frequency alternating voltage  $u_i$ , the excitation current  $i_i$ , output voltage  $u_{\sin}$ , and  $u_{\cos}$  can be expressed as follows:

$$\begin{cases} i_i = \frac{u_i}{j\omega L_1} \\ u_{\sin} = j\omega M_s i_i = \frac{M_s}{L_1} u_i = k u_i \sin \theta_e \\ u_{\cos} = j\omega M_c i_i = \frac{M_c}{L_1} u_i = k u_i \cos \theta_e \end{cases} \quad (4)$$

where  $\theta_e = \omega_e t$  is the electrical angle and  $k = M_m / L_1$  is the conversion ratio of the resolver.

Finally, the envelopes of the sine and cosine output signals,  $u_s$  and  $u_c$ , are extracted, as shown in Figure 3. Through the inverse tangent operation, the rotor position of the resolver is obtained:

$$\theta_e = \arctan\left(\frac{u_s}{u_c}\right) \quad (5)$$

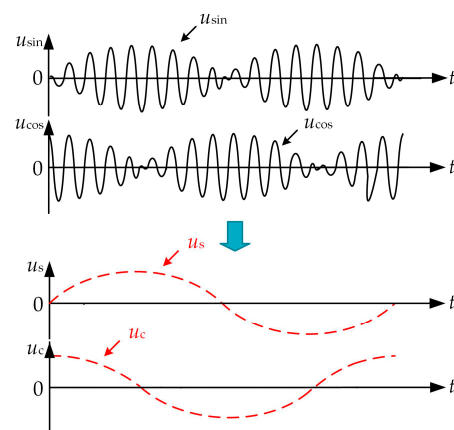


Figure 3. Output waveforms and envelope of the Conventional resolver.

### 3. Proposed VR Resolver with Three-Phase Symmetrical Windings

#### 3.1. Design Method of the Proposed VR (Variable Reluctance) Resolver

In order to design the winding arrangement of the resolver into three symmetrical windings instead of orthogonal windings and to ensure that the windings do not overlap distribution, it is necessary to make the three sets of windings of the resolver in the spatial phase of the difference of  $120^\circ$  electrical angle, and the stator windings in each stator tooth only exist in a winding, which in turn achieves the purpose of easing the manufacturing process of the resolver. The structural diagram of the proposed resolver is depicted in Figure 4, featuring three sets of windings, namely the A-phase windings S1S4, B-phase windings S2S5, and C-phase windings S3S6.

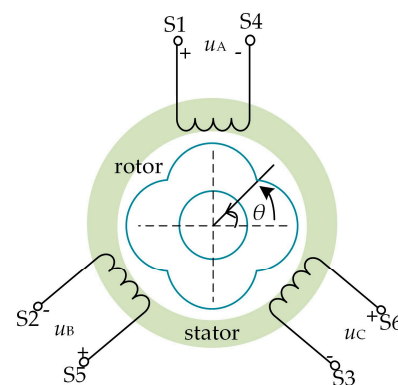


Figure 4. Structure of the proposed VR resolver.

Taking the 4-rotor saliencies (4-X) resolver as an example, its main parameters are shown in Table 1, and the specific design process is as follows:

1. Selection of main dimensions

**Table 1.** Main parameters of the proposed resolver.

Parameters	Sizes
Outer diameter of the stator	65.8 mm
Inner diameter of stator	55.8 mm
Minimum air gap length	0.6 mm
Number of stator teeth	12
Number of rotor pole pairs	4
Stator thickness	4 mm
Rotor thickness	6 mm
Stator tooth width	7 mm
Number of turns per tooth	40
Excitation frequency	100 kHz
Excitation inductance	230 $\mu$ H~295 $\mu$ H

The main dimensions of the resolver include the outer diameter of the stator, the inner diameter of the stator, the minimum air gap length, the thickness of the stator and rotor, etc. The specific dimensions need to be matched according to the size of the motor.

2. Selection of stator teeth

If the resolver is designed as a three-phase symmetrical winding, it is necessary to ensure that the A, B, and C three-phase windings are distributed at an electrical angle of  $120^\circ$  in spatial position. The calculation formula for the number of teeth is:

$$Z_s = \frac{P \cdot 2\pi}{2\pi/3} = 3P \quad (6)$$

Therefore, the number of stator teeth needs to be three times the number of polar pairs. Taking a 4-X resolver as an example, the number of stator teeth should be selected as 12.

3. Winding method and distribution of winding

There are three groups of windings: A phase, B phase, and C phase. The three groups of windings are symmetrically identical in winding method and arrangement, with a spatial phase difference of  $120^\circ$  in electrical angle. Each stator tooth has only one winding on the stator winding. Each phase winding is wound every two teeth, while the winding between the phases is wound around the adjacent teeth. The winding direction and number of turns under all teeth are the same. The specific winding arrangement is shown in Figures 5 and 6.

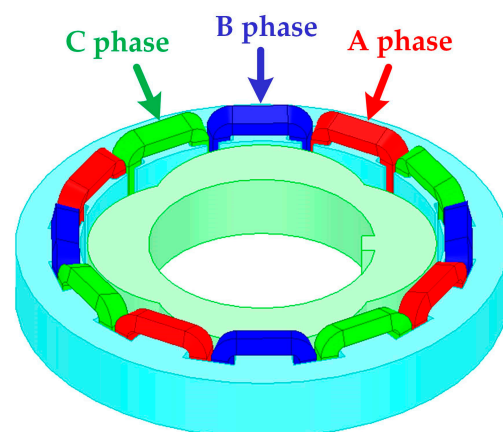


**Figure 5.** 4-X VR resolver.

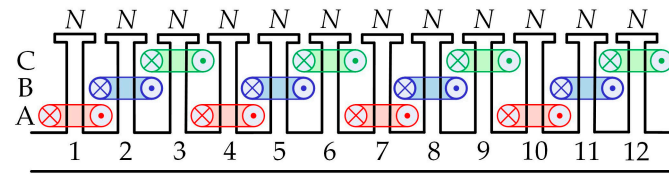


Figure 6. Winding distribution of a 4-X VR resolver.

#### 4. Selection of permeable material

To improve the accuracy of the resolver and reduce losses, materials with high impedance, high magnetic permeability, and high initial magnetic permeability should be selected. Magnetic materials such as iron-nickel soft magnetic alloys (1J79, 1J50) and silicon steel sheets (D42, DG41) have good magnetic and electrical properties and are widely used as stamping materials for resolvers. Considering the comprehensive material properties, this paper uses 1J79 as the manufacturing material for the resolver.

#### 5. Rotor-shaped design

The shape of the rotor of the resolver is determined by the length of the air gap, which varies cosine-wise with the rotation angle of the resolver. Ideally, the length of the air gap should satisfy the following:

$$\delta_\theta = \frac{\delta_1}{1 + (\frac{\delta_1}{\delta_0} - 1) \cos P\theta} \tag{7}$$

where  $\delta_1/\delta_0$  is the rotor sinusoidal coefficient. Generally, to obtain a satisfactory rotor, it is often necessary to repeatedly optimize parameters such as the minimum air gap length and sine coefficient, as well as eliminate rotor harmonics through harmonic injection and other methods. To obtain a relatively sinusoidal output voltage, a rotor with a sinusoidal coefficient of 1.3 is finally chosen in this paper for the simulation.

#### 6. Determination of winding turns

The design basis for the number of turns of the resolver is related to the input impedance. Generally, it is required that the input impedance be greater than 120  $\Omega$ ; too low an input impedance can lead to excessive excitation current, resulting in magnetic saturation of the resolver and distortion of the output signal; too high an input impedance can lead to an increase in the number of turns, which can still increase the difficulty of the resolver manufacturing process. The initial selection of the number of turns can be referred to using the following formula:

$$\begin{cases} W_s = \sqrt{\frac{K_i Z_{oc} \delta_1 P \times 10^9}{0.4 \pi^2 f \alpha_\delta \tau_\delta l_\delta}} \\ \delta_e = K_\mu K_\delta \delta_0 \\ \tau_\delta = \frac{\pi D_\delta}{2P} \\ D_\delta = \frac{D_{i1} + D_{e2}}{2} \\ K_\delta = \frac{t_1 + 10\delta_0}{t_1 + 10\delta_0 - b_{01}} \\ t_1 = \frac{\pi D_{i1}}{Z_s} \end{cases} \tag{8}$$

wherein  $W_s$  is the total number of turns of the excitation winding,  $K_i$  is the potential coefficient,  $K_\mu$  is the magnetic saturation coefficient,  $Z_{oc}$  is the open-circuit input impedance,  $\delta_e$  is the equivalent air gap,  $\delta_0$  is the minimum air gap length,  $f$  is the excitation frequency,  $\alpha_\delta$  is the pole arc coefficient,  $t_\delta$  is the pole pitch,  $l_\delta$  is the axial length of the air gap,  $D_\delta$  is the average diameter of the air gap,  $t_1$  is the tooth pitch,  $D_{i1}$  is the inner diameter of the stator,  $D_{e2}$  is the outer diameter of the rotor, and  $b_{01}$  is the slot width.

Since the input impedance of this particular structure of the resolver proposed in this paper varies with the rotor position, the initial input impedance is chosen to be 150  $\Omega$  in

order to ensure that its minimum input impedance is greater than  $120 \Omega$ . However, the initial reference number of turns obtained through formula calculation is only an initial reference, and subsequent optimization analysis of parameters is required to obtain the final number of turns. Finally, the number of turns under each tooth is selected to be 40, which is in line with the design requirements, as shown in the subsequent simulation results and prototype testing results.

The finite element Maxwell2D simulation model of the proposed resolver is shown in Figure 7, and its simulation parameters are fully consistent with the design parameters. The field line distribution of the proposed resolver excitation with phase A is shown in Figure 8. It can be seen that the phase A winding (red winding) is distributed on the 1st, 4th, seventh, and 10th teeth. The magnetic field lines stimulated by itself are closed through the adjacent teeth, and the adjacent B-phase and C-phase will induce output voltage. The flux density map of the proposed resolver is shown in Figure 9. From the magnetic density value, it can be seen that the magnetic load of the resolver is very low, so there is no magnetic saturation.

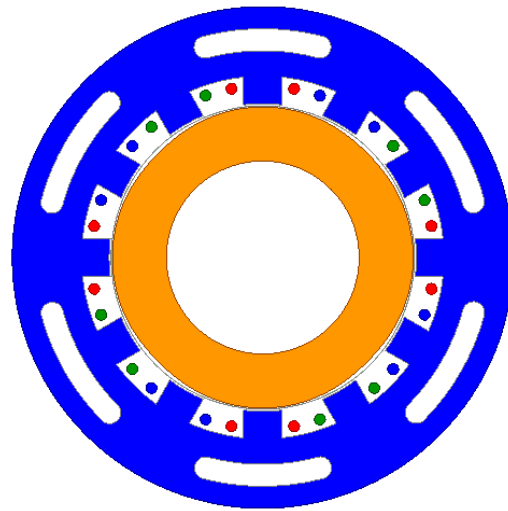


**Figure 7.** Simulation model of the proposed resolver.

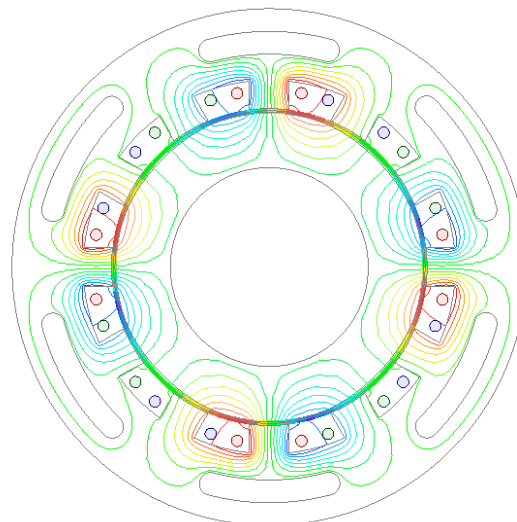


**Figure 8.** Field line distribution of the proposed resolver.

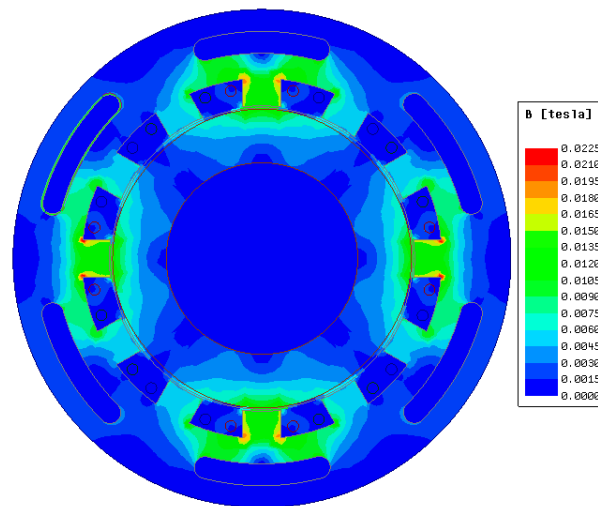


**Figure 9.** Flux density map of the proposed resolver.

### 3.2. Theoretical Derivation of Output Voltage and Finite Element Analysis

The magnetic permeance under different teeth of the resolver is the same as that in Equation (1), and neglecting its higher harmonics, the sum of the magnetic permeances under all teeth corresponding to A, B, and C is:

$$\left\{ \begin{array}{l} \sum_{i=1,4,7\dots}^{Z_s} \Lambda_{Ai} = P\Lambda_0 + P\Lambda_1 \cos(P\theta) \\ \sum_{i=2,5,8\dots}^{Z_s} \Lambda_{Bi} = P\Lambda_0 + P\Lambda_1 \cos(P\theta + 2\pi/3) \\ \sum_{i=3,6,9\dots}^{Z_s} \Lambda_{Ci} = P\Lambda_0 + P\Lambda_1 \cos(P\theta - 2\pi/3) \end{array} \right. \quad (9)$$

The input reactances of A, B, and C phases are, respectively:

$$\left\{ \begin{array}{l} X_A = j\omega_t N_f^2 [P\Lambda_0 + P\Lambda_1 \cos(P\theta)] \\ X_B = j\omega_t N_f^2 [P\Lambda_0 + P\Lambda_1 \cos(P\theta + 2\pi/3)] \\ X_C = j\omega_t N_f^2 [P\Lambda_0 + P\Lambda_1 \cos(P\theta - 2\pi/3)] \end{array} \right. \quad (10)$$

It can be seen that the input impedance of the A, B, and C phases varies according to the change in rotor position angle. Thus, the expressions for the self-inductance of the resolvers A, B, and C, as well as the mutual inductance between A, B, and C, can be obtained as follows:

$$\left\{ \begin{array}{l} L_A = L_0 + L_1 \cos(P\theta) \\ L_B = L_0 + L_1 \cos(P\theta + 2\pi/3) \\ L_C = L_0 + L_1 \cos(P\theta - 2\pi/3) \end{array} \right. \quad (11)$$

$$\left\{ \begin{array}{l} M_{AB} = M_{BA} = -M_0 - M_1 \cos(P\theta - 2\pi/3) \\ M_{BC} = M_{CB} = -M_0 - M_1 \cos(P\theta) \\ M_{CA} = M_{AC} = -M_0 - M_1 \cos(P\theta + 2\pi/3) \end{array} \right. \quad (12)$$

where  $L_A$ ,  $L_B$ , and  $L_C$  are the self-inductances of the three windings A, B, C, and  $M_{AB}$ ,  $M_{BA}$ ,  $M_{BC}$ ,  $M_{CB}$ ,  $M_{AC}$ , and  $M_{CA}$  are the mutual inductances between AB, BC, and CA phases. The finite element simulation waveforms of self-inductance and mutual induction are presented in Figures 10 and 11, which show good agreement with theoretical analysis. In the simulation, the rotational speed of the resolver is 3000 r/min. From Equations (11) and (12), it can be seen that the proposed inductance theory of the resolver is similar to the main winding inductance of the IPMSM, with a phase difference of  $120^\circ$  electrical angle [22]. However, the difference is that the inductance of the IPMSM varies

at twice the frequency as the rotor position of the motor changes. Since the rotor of the resolver does not have permanent magnets or magnetic poles, the inductance of the resolver shows a single octave variation with the rotor position, which is more conducive to the application of the rotor position detection technique for IPMSM under power failure and restarted conditions to the proposed resolver.

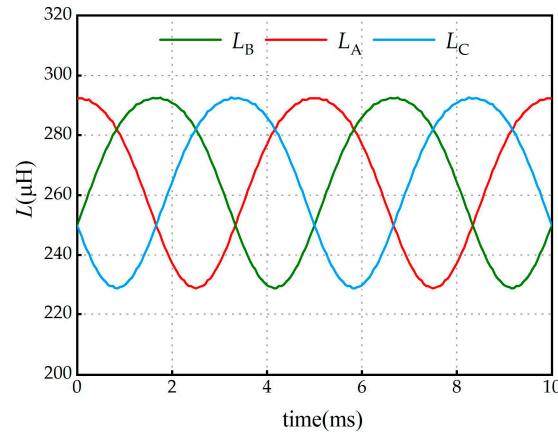


Figure 10. Simulated waveforms of three self-inductances of the proposed resolver.

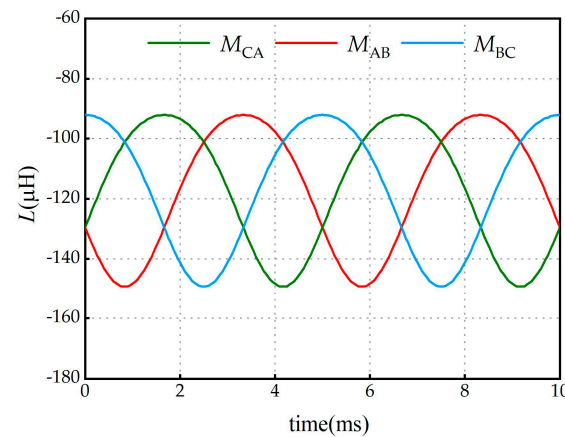


Figure 11. Simulated waveforms of phase-to-phase mutual inductance of the proposed resolver.

The proposed equivalent wind model of the resolver is shown in Figure 12. If excitation voltage  $u_i$  is injected into phase A, the output voltage of phases B and C can be expressed as shown in Equation (13), and the finite element simulation waveform of its output voltage envelope is shown in Figure 13.

$$\begin{cases} u_B = j\omega_t M_{AB} i_{exc} = \frac{M_{AB}}{L_A} u_{exc} \\ u_C = j\omega_t M_{AC} i_{exc} = \frac{M_{AC}}{L_A} u_{exc} \end{cases} \quad (13)$$

When injecting excitation voltage  $u_i$  into phase B, the output voltage of phases A and C can be expressed as shown in Equation (14), and the finite element simulation waveform of its output voltage envelope is shown in Figure 14.

$$\begin{cases} u_A = j\omega_t M_{BA} i_{exc} = \frac{M_{BA}}{L_B} u_{exc} \\ u_C = j\omega_t M_{BC} i_{exc} = \frac{M_{BC}}{L_B} u_{exc} \end{cases} \quad (14)$$

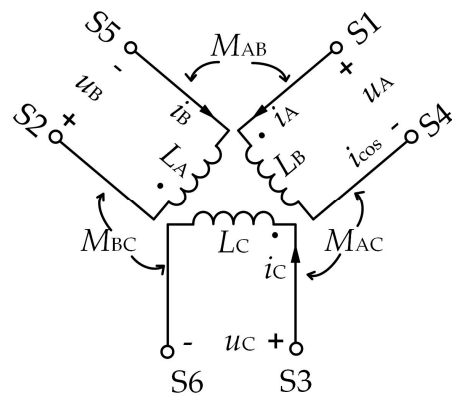


Figure 12. Equivalent winding model of the proposed resolver.

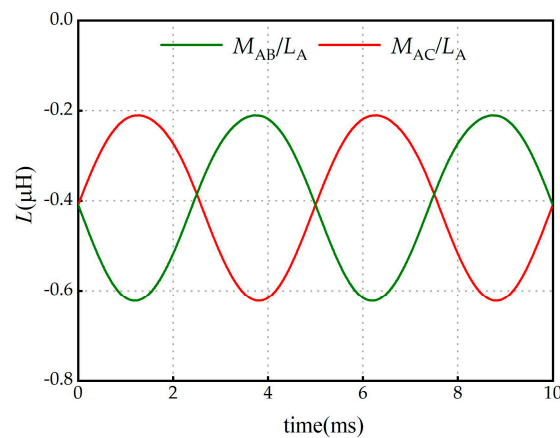


Figure 13. Simulation waveform of the B and C output voltage envelopes.

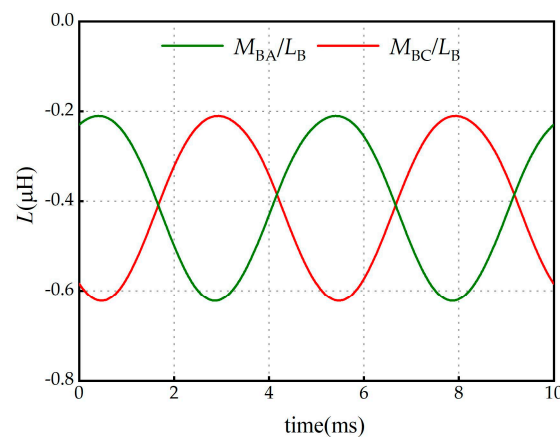


Figure 14. Simulation waveform of the A and C output voltage envelopes.

### 3.3. The RDC Method Used

This paper refers to the rotor position detection technology of IPMSM during power-off and restart for position calculation. Using the inductance characteristics of the resolver, which change at a single frequency over one electrical cycle, it is possible to obtain the absolute rotor position within the range of  $[0, 2\pi]$ . This is significantly different from the method of determining the polarity of the motor by using the inductance characteristics, which change at double the frequency over one electrical cycle. The RDC method changes the conventional RDC method on the proposed resolver, making it possible to calculate the rotor position without extracting the orthogonal envelope.

The frequency division excitation method is used for the resolver. The system structure of the RDC method is shown in Figure 15, and the excitation timing diagram is shown in

Figure 16. Different windings are excited at different control cycles, and the average of the output voltages of the remaining two phases is detected. The average value is processed as a ratio, and the rotor position is solved using the ratio of the average value of the output voltage of the current control cycle and the average value of the output voltage of the previous control cycle. The principle of implementation is as follows:

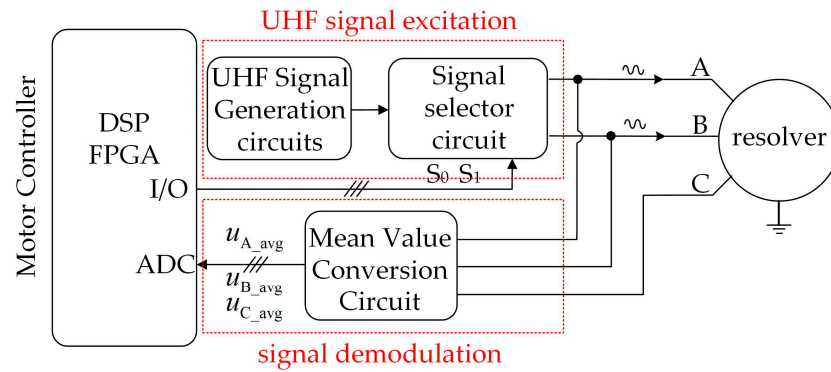


Figure 15. System structure of the resolver-to-digital conversion method.

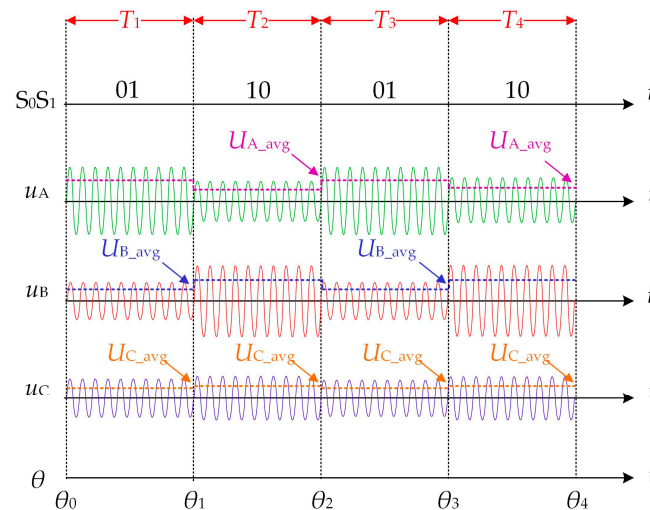


Figure 16. Timing sequence of the ultra-high frequency sinusoidal signal injection.

Since its A, B, and C phase windings are structurally identical, it is possible to perform A-phase excitation at the  $T_1$  control cycle. The Digital Signal Processor controller sends out the selector signal  $S_0S_1 = 01$ , which drives the signal selector circuit to inject the UHF signal into the A-phase winding  $S_1S_4$ . The average of the output voltages  $u_B$  and  $u_C$  of phases B and C is detected, and then their output voltages are divided to obtain  $k_1$ . B-phase excitation is performed during the  $T_2$  control cycle, and the DSP controller sends out a selector signal with  $S_0S_1 = 10$ , which drives the signal-selector circuit to inject a UHF signal into the B-phase winding  $S_2S_5$ . Detect the average value of the output voltages  $u_A$  and  $u_C$  of phases A and C, and then divide their output voltages to obtain  $k_2$ . Repeat  $T_1$  and  $T_2$  in subsequent control cycles. The expressions for  $k_1$  and  $k_2$  are:

$$\begin{cases} k_1 = \frac{U_{B\_avg}}{U_{C\_avg}} = \frac{M_{AB}}{M_{AC}} = \frac{-M_0 - M_1 \cos(P\theta - 2\pi/3)}{-M_0 - M_1 \cos(P\theta + 2\pi/3)} \\ k_2 = \frac{U_{A\_avg}}{U_{C\_avg}} = \frac{M_{BA}}{M_{BC}} = \frac{-M_0 - M_1 \cos(P\theta - 2\pi/3)}{-M_0 - M_1 \cos(P\theta)} \end{cases} \quad (15)$$

By simplifying and arranging, the rotor position expression can be obtained as follows:

$$\theta_t = \arctan \frac{\frac{3}{2}k_2(k_1 - 1)}{\sqrt{3}(k_1 - \frac{1}{2}k_2 - \frac{1}{2}k_1k_2)} \quad (16)$$

From Equation (16), it can be seen that this function can only obtain the rotor position in the range of  $[-\pi/2, \pi/2]$ . Since  $k_1$  represents the ratio of  $U_{B\_avg}$  to  $U_{C\_avg}$ , it represents the ratio of  $M_{AB}$  to  $M_{AC}$ . When  $M_{AB} = M_{AC}$ ,  $k_1 = 1$ , and the rotor position is  $0^\circ$  and  $180^\circ$ . Therefore, by determining the relationship between  $k$  and 1, it can be extended to the rotor position in the range of  $[0, 2\pi]$ , and the complete position angle  $\theta_r$  over the entire electrical cycle can be obtained as shown in Equation (17):

$$\theta_r = \begin{cases} \theta_t & k_1 < 1, \theta_e > 0 \\ \theta_t + \pi & k_1 < 1, \theta_e < 0 \\ \theta_t + \pi & k_1 > 1, \theta_e > 0 \\ \theta_t + 2\pi & k_1 > 1, \theta_e < 0 \end{cases} \quad (17)$$

#### 4. Experimental Results and Analysis

In order to verify the feasibility of the proposed resolver, an experimental platform is built, as shown in Figure 17.

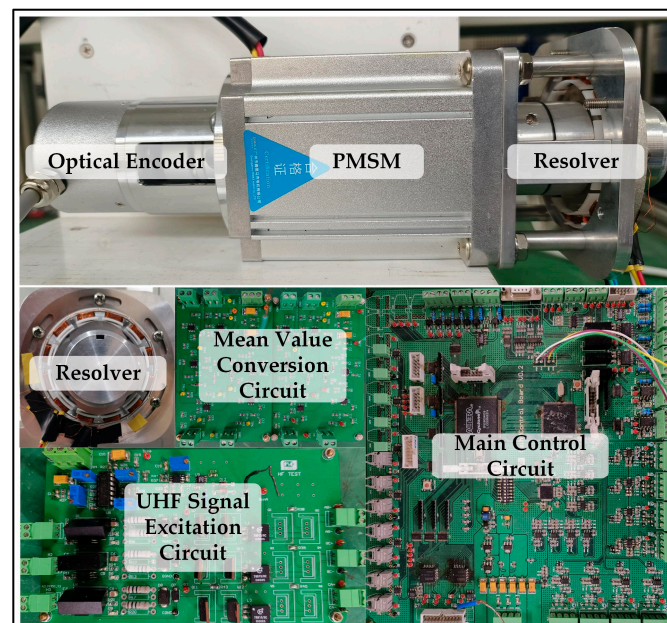


Figure 17. Experimental system.

On the platform, a DSP (TMS320F28335) clocked at 150 MHz is used in the control unit to sample the demodulated envelope of the output signal and calculate the rotor position. In addition, the waveforms of the demodulation envelope and rotor position measured in the experiment were output for observation using a DAC. Peripheral circuits are used to generate the excitation signal of the resolver, amplification of the excitation signal, selectivity of the excitation signal, and demodulation of the output signal of the resolver. The resolver is mounted on a 750 W PMSM with four pairs of poles and a rated speed of 3000 r/min.

The resolver used in the experiment is a handmade resolver. The specific parameters of the resolver and the previous design parameters are basically the same; the windings are hand-wound with 0.1 mm enameled wire; the physical picture is shown in Figure 18. A UHF sinusoidal signal of 100 kHz with an amplitude of 4 V was used as the excitation signal. The number of pole pairs of the resolver is equal to the number of pole pairs of the

motor, so the rotor electrical angle of the test motor is equal to the rotor electrical angle of the resolver. In addition, an optical encoder of 2500 lines was mounted coaxially with the motor for comparison of experimental results, and its sampled measurements were used as the actual position, denoted as  $\theta_0$ .



**Figure 18.** Prototype of the produced resolver.

The software design in this article is illustrated in Figure 19, where the GPIO ports of the DSP are initialized and configured to output high and low electrical levels as the strobe signal S0S1 for frequency division excitation during different control cycles. If an excitation signal is applied to the A-phase winding during the  $T_1$  control cycle, and when the algorithm for applying an excitation signal to the B-phase winding during the  $T_2$  control cycle is initiated, the sampling results of the B-phase and C-phase at the end of the previous control cycle (i.e., at the end of the  $T_1$  control cycle) are read using an ADC module, and the rotor position for the current control cycle is calculated based on these sampling results. When an excitation signal is reapplied to the A-phase winding during the  $T_3$  control cycle, the sampling results of the A-phase and C-phase at the end of the  $T_2$  control cycle are read using an ADC module, and the rotor position for the current control cycle is calculated based on these sampling results. This process is repeated, and the rotor position of the resolver proposed in this paper can be obtained.

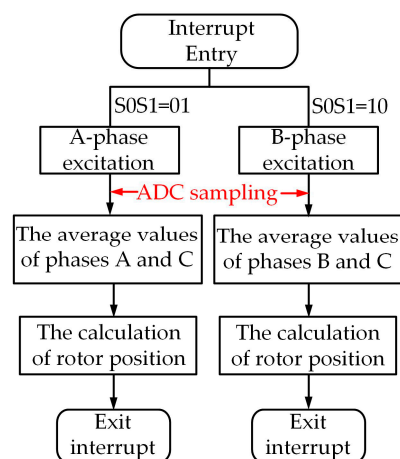


**Figure 19.** Software program flow chart.

As shown in Figure 20, a UHF sinusoidal signal is injected into phase A of the resolver during the control cycle  $T_1$ , at which time the average values of the output voltages of phases B and C are detected to be 558 mV and 575 mV, respectively, and at this time they have a ratio  $k_1 = 0.97$ . The UHF sinusoidal signal is injected into phase B of the rotary transformer during the control cycle  $T_2$ , at which time the average values of the output voltages of phase A and C are detected to be 500 mV and 781 mV, respectively, at which time their ratio  $k_2 = 0.64$ . Taking into Equation (16), the rotor position  $\theta_r = 3.091$  rad for the  $T_2$  control cycle can be calculated, which is almost the same as the 3.093 rad in the experiment. The  $T_3$  control cycle injected UHF sinusoidal signals into phase A repeatedly. At this time, the average output voltages of the detected phases B and C were 565 mV and

544 mV, respectively. Their ratio,  $k_1$ , was calculated as 1.0386 using Equation (16). The rotor position of the  $T_3$  control cycle,  $\theta_r$ , was calculated as 3.195 rad, which is almost the same as the 3.184 rad obtained from experiments. This verifies the accuracy of the rotor position obtained using this method. This process is repeated for  $T_4$  and all subsequent control cycles to determine the rotor position for each cycle.

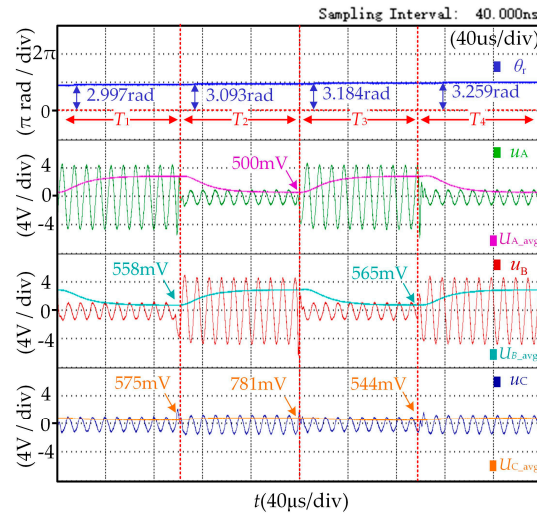


Figure 20. Excitation and output signals and their average values for each phase at 2000 r/min.

As shown in Figure 21, the estimated position, actual position,  $k_1$ , B-phase and C-phase demodulation envelopes, and A-phase and C-phase demodulation envelopes are shown in order from top to bottom at 300 r/min. Where  $U_{A\_avg}$ ,  $U_{B\_avg}$ , and  $U_{C\_avg}$  are the average values of the output voltages of phases A, B, and C, respectively. As can be seen from the figure, the estimated position can accurately track the actual position. Consistent with the theoretical analysis, when  $k_1 = 1$ , this time the rotor position is  $0^\circ$ . At this point is also the intersection of the B-phase envelope and the C-phase envelope, and by judging the relationship between the sizes of  $k_1$  and 1, you can obtain the exact rotor position of the entire electrical cycle. Figures 22 and 23 show the estimated position, actual position,  $k_1$ , B-phase and C-phase envelope, and A-phase and C-phase envelope at 1500 r/min as well as 3000 r/min, respectively. The experimental results in the full-speed domain are consistent with the theoretical analysis, verifying the feasibility of the RDC.

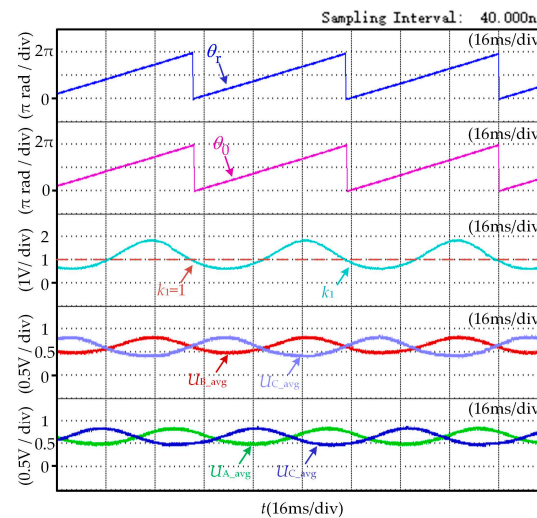


Figure 21. Estimated position, actual position,  $k_1$  and demodulation envelope at 300 r/min.

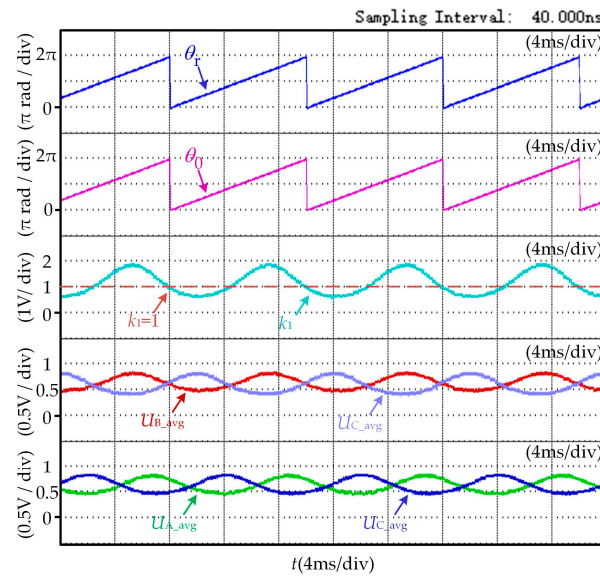


Figure 22. Estimated position, actual position,  $k_1$  and demodulation envelope at 1500 r/min.

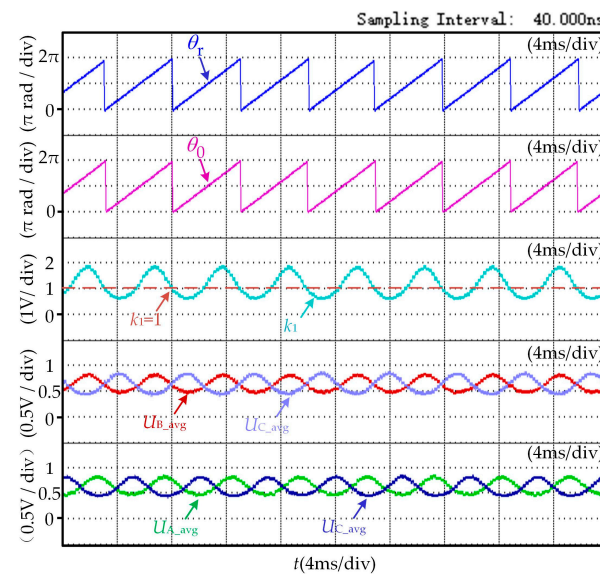
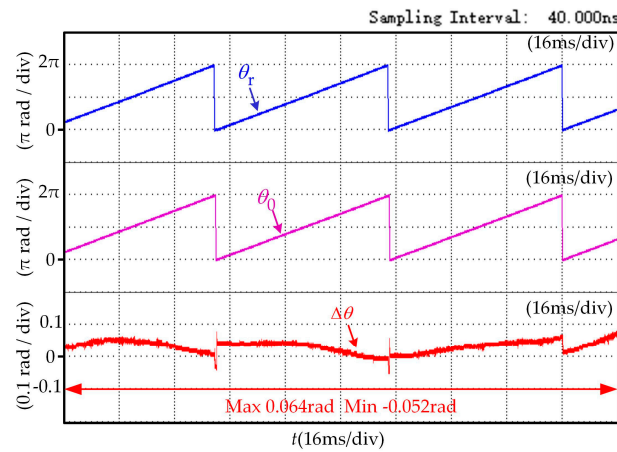
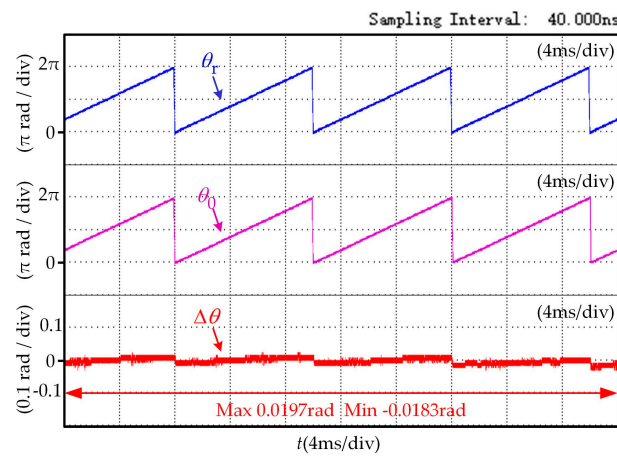


Figure 23. Estimated position, actual position,  $k_1$ , and demodulation envelope at 3000 r/min.

As shown in Figure 24, which represents estimated position, actual position, and rotor position error at 300 r/min in the low-speed zone, it can be seen that the minimum value of rotor position error at this speed is  $-0.052$  rad, and the maximum value is  $0.064$  rad. As shown in Figure 25, the maximum rotor position error is  $0.0197$  rad, and the minimum rotor position error is  $-0.0183$  rad when the motor speed is at a speed of 1500 r/min. As shown in Figure 26, when the rotational speed is at the rated speed of 3000 r/min, the maximum rotor position error is  $0.098$  rad, and the minimum rotor position error is  $-0.106$  rad. It can be seen that the positional accuracy at different rotational speeds meets most of the industrial requirements, verifying the accuracy of the RDC.



**Figure 24.** Estimated position, actual position, and rotor position errors of the proposed resolver at 300 r/min.



**Figure 25.** Estimated position, actual position, and rotor position errors of the proposed resolver at 1500 r/min.

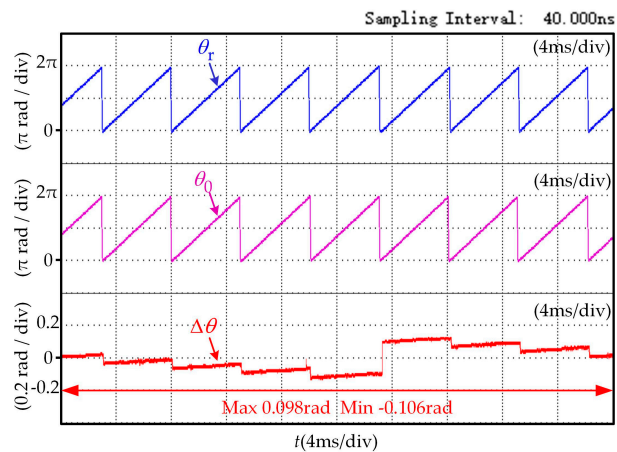


**Figure 26.** Estimated position, actual position, and rotor position errors of the proposed resolver at 3000 r/min.

Based on the analysis of the experimental results, it is concluded that when one phase of the three-phase winding of the resolver is designated as the excitation phase, two demodulation envelopes can be obtained by detecting the average values of the other two phases. Due to the alternate excitation of the A-phase winding or B-phase winding in different control cycles, there are a total of four envelope curves, namely two sets of

envelope curves. By comparing each set of envelope curves, the ratios  $k_1$  and  $k_2$  can be obtained. Utilizing  $k_1$  and  $k_2$ , the rotor position can be calculated. The experimental results at motor speeds of 300 r/min, 1500 r/min, and 3000 r/min demonstrate the feasibility of the proposed resolver and the RDC method. Furthermore, the error between the estimated rotor position and the actual rotor position at these speeds indicates the accuracy of the RDC method. Therefore, the proposed VR resolver with three-phase symmetric windings can achieve a relatively accurate rotor position under the RDC method using frequency division excitation. The proposed resolver with three-phase symmetric windings breaks the limitation of conventional resolvers, which output orthogonal signals, while easing the structure of conventional resolvers. Moreover, the excitation method has been changed from single-phase excitation to frequency-divided excitation, which is the most significant difference from conventional VR resolvers.

## 5. Conclusions

A novel VR resolver with symmetrical three-phase windings is proposed in this paper. The winding directions and turns under all teeth of the proposed resolver are the same, and the windings are not overlapped, which eases the structure and manufacturing process of the VR resolver. Secondly, the RDC method of the proposed resolver references the UHF injection method for the IPMSM under power-off and restarted conditions. The absolute rotor position for the entire electrical cycle can be obtained instead of extracting the conventional orthogonal envelope. Finally, a 4-X resolver prototype is fabricated and experimentally tested. The feasibility of the proposed resolver and the accuracy of the RDC were verified by experimental results. In the current research on VR resolvers, the majority of the resolvers still possess relatively complex structures. However, the simpler non-overlapping winding resolvers, including the VR resolvers proposed in this paper based on three-phase windings, all exhibit issues such as low coupling coefficients and insufficient signal-to-noise ratios in their output signals. These issues may potentially affect the precision of rotor position detection, thus requiring further research.

**Author Contributions:** Data curation, J.C.; investigation, X.L. and Z.Z.; methodology, J.C. and Z.Z.; project administration, Z.Z.; resources, X.L.; validation, X.L. and J.C.; writing—original draft, J.C.; writing—review and editing, X.L. All authors have read and agreed to the published version of the manuscript.

**Funding:** This research was funded by “Zhejiang Provincial Natural Science Foundation of China under Grant No. LQ22E070008”, “The National Natural Science Foundation of China under Grant No. 52077155”.

**Data Availability Statement:** The original contributions presented in the study are included in the article, further inquiries can be directed to the corresponding author.

**Conflicts of Interest:** The authors declare no conflicts of interest.

## Nomenclature

### A. List of Acronyms

VR	Variable Reluctance
PMSM	Permanent Magnet Synchronous Motors
RDC	Resolver-to-Digital Conversion
UHF	Ultra-High Frequency
IPMSM	Internal Permanent Magnet Synchronous Motors
4-X	4-rotor saliencies

### B. List of Symbols (conventional VR resolver)

$\Lambda_i$	Magnetic permeability under a certain tooth
$\Lambda_0$	The base value of magnetic permeability
$\Lambda_\mu$	$\mu$ th conductivity harmonic component amplitude

$\mu$	The order of harmonic content
$N$	Number of turns of excitation winding
$f$	Excitation frequency
$X$	Input reactance
$\omega$	Excitation angular frequency
$L_1, L_2$	Excitation inductance and output inductance
$u_i$	Excitation voltage
$i_i$	Excitation current
$u_{\sin}, u_{\cos}$	Sine-cosine winding output voltage
$M_s, M_c$	Mutual inductance between excitation and output windings
$\theta_e$	Rotor mechanical and electrical angles
$P$	Number of rotor pole pairs
$Z_s$	The number of stator teeth
$k$	Resolver conversion ratio
$u_s, u_c$	Sine-cosine demodulated signal
C. List of Symbols (proposed VR resolver)	
$P$	Number of rotor pole pairs
$\theta$	Rotor mechanical angle
$Z_s$	Number of stator teeth
$\delta_\theta$	Air gap length
$\delta_0 \delta_1$	Air gap length for $0^\circ$ electrical angle and $90^\circ$ electrical angle
$W_s$	Total turns of winding
$K_i$	Potential factor
$K_\mu$	Magnetic circuit saturation factor
$Z_{oc}$	Open-circuit input impedance
$\delta_e$	Equivalent air gap length
$\alpha_\delta$	Polar arc coefficient
$\tau_\delta$	Polar distance
$l_\delta$	Air Gap Axial Length
$D_\delta$	Average air gap diameter
$t_1$	Tooth pitch
$D_{i1}$	Stator inner diameter
$D_{e2}$	Rotor outer diameter
$b_{01}$	Notch width
$\Lambda_{Ai}, \Lambda_{Bi}, \Lambda_{Ci}$	Air gap permeability under the $i$ th tooth of phases A, B, and C
$X_A, X_B, X_C$	Input reactance of phases A, B and C
$\omega_t$	Excitation angular frequency
$N_t$	Number of turns of winding under each tooth
$L_A, L_B, L_C$	Self-inductance of phase A, B and C windings
$L_0, L_1$	Self-induced base value and self-induced base wave component amplitude
$M_{AB}, M_{BA}$	Mutual inductance between phase A and B windings
$M_{AC}, M_{CA}$	Mutual inductance between phase A and C windings
$M_{BC}, M_{CB}$	Mutual inductance between phase B and C windings
$M_0, M_1$	Mutual inductance fundamental value and mutual inductance fundamental component amplitude
$u_{exc}$	Excitation voltage
$i_{exc}$	Excitation Current
$u_A, u_B$	A and B phase output voltage
$U_{A\_avg}, U_{B\_avg}, U_{C\_avg}$	Average of output voltages of phases A, B and C
$k_1$	Ratio of average value of output voltage of phase B and C
$k_2$	Ratio of average value of output voltage of phase A and C
$\theta_i$	Rotor electrical angle in the interval $[-\pi/2, \pi/2]$

## References

1. Luan, M.; Zhang, Y.; Li, X.; Xu, F. A Rotor Position Detection Method for Permanent Magnet Synchronous Motors Based on Variable Gain Discrete Sliding Mode Observer. *World Electr. Veh. J.* **2024**, *15*, 87. [[CrossRef](#)]
2. Li, Y.; Hu, H.; Shi, P. A Review of Position Sensorless Compound Control for PMSM Drives. *World Electr. Veh. J.* **2023**, *14*, 34. [[CrossRef](#)]
3. Wang, Z.; Yao, B.; Guo, L.; Jin, X.; Li, X.; Wang, H. Initial Rotor Position Detection for Permanent Magnet Synchronous Motor Based on High-Frequency Voltage Injection without Filter. *World Electr. Veh. J.* **2020**, *11*, 71. [[CrossRef](#)]
4. Wang, Z.; Du, D.; Yu, Q.; Zhang, H.; Li, C.; Guo, L.; Gu, X.; Li, X. Sensorless Control Method of High-Speed Permanent Magnet Synchronous Motor Based on Discrete Current Error. *World Electr. Veh. J.* **2023**, *14*, 69. [[CrossRef](#)]
5. Nasiri-Gheidari, Z.; Tootoonchian, F. Influence of mechanical faults on the position error of an axial flux brushless resolver without rotor windings. *IET Electr. Power Appl.* **2017**, *11*, 613–621. [[CrossRef](#)]
6. Murray, A.; Hare, B.; Hirao, A. Resolver position sensing system with integrated fault detection for automotive applications. In Proceedings of the SENSORS, 2002 IEEE, Orlando, FL, USA, 12–14 June 2002; pp. 864–869. [[CrossRef](#)]
7. Alipour-Sarabi, R.; Nasiri-Gheidari, Z.; Tootoonchian, F.; Oraee, H. Effects of Physical Parameters on the Accuracy of Axial Flux Resolvers. *IEEE Trans. Mag.* **2017**, *53*, 1–11. [[CrossRef](#)]
8. Ge, X.; Zhu, Z.Q.; Ren, R.; Chen, J.T. A Novel Variable Reluctance Resolver for HEV/EV Applications. *IEEE Trans. Ind. Appl.* **2016**, *52*, 2872–2880. [[CrossRef](#)]
9. Tootoonchian, F. Design, Performance, and Testing of a Brushless Axial Flux Resolver Without Rotor Windings. *IEEE Sens. J.* **2016**, *16*, 7464–7471. [[CrossRef](#)]
10. Xiao, L.; Li, Z.; Bi, C. An Optimization Approach to Variable Reluctance Resolver. *IEEE Trans. Magn.* **2020**, *56*, 1–5. [[CrossRef](#)]
11. Figueiredo, J. Resolver Models for Manufacturing. *IEEE Trans. Ind. Electron.* **2011**, *58*, 3693–3700. [[CrossRef](#)]
12. Tootoonchian, F. Proposal of a New Affordable 2-Pole Resolver and Comparing Its Performance with Conventional Wound-Rotor and VR Resolvers. *IEEE Sens. J.* **2018**, *18*, 5284–5290. [[CrossRef](#)]
13. Sun, L. Analysis and Improvement on the Structure of Variable Reluctance Resolvers. *IEEE Trans. Magn.* **2008**, *44*, 2002–2008. [[CrossRef](#)]
14. Kim, K.-C. Analysis on the Characteristics of Variable Reluctance Resolver Considering Uneven Magnetic Fields. *IEEE Trans. Magn.* **2013**, *49*, 3858–3861. [[CrossRef](#)]
15. Kim, K.-C.; Jin, C.S.; Lee, J. Magnetic Shield Design Between Interior Permanent Magnet Synchronous Motor and Sensor for Hybrid Electric Vehicle. *IEEE Trans. Magn.* **2009**, *45*, 2835–2838. [[CrossRef](#)]
16. Xiao, L.; Bi, C. An optimization approach of rotor contour for variable reluctance resolver. *CES Trans. Electr. Mach. Syst.* **2021**, *5*, 257–261. [[CrossRef](#)]
17. Jin, C.-S.; Jang, I.-S.; Bae, J.-N.; Lee, J.; Kim, W.-H. Proposal of Improved Winding Method for VR Resolver. *IEEE Trans. Magn.* **2015**, *51*, 1–4. [[CrossRef](#)]
18. Saneie, H.; Nasiri-Gheidari, Z.; Tootoonchian, F. Accuracy Improvement in Variable Reluctance Resolvers. *IEEE Trans. Energy Convers.* **2019**, *34*, 1563–1571. [[CrossRef](#)]
19. Kim, K.-C.; Hwang, S.-J.; Sung, K.-Y.; Kim, Y. A study on the fault diagnosis analysis of variable reluctance resolver for electric vehicle. In Proceeding of the SENSORS, 2010 IEEE, Waikoloa, HI, USA, 1–4 November 2010; pp. 290–295. [[CrossRef](#)]
20. Ge, X.; Zhu, Z.Q.; Ren, R.; Chen, J.T. A Novel Variable Reluctance Resolver with Nonoverlapping Tooth–Coil Windings. *IEEE Trans. Energy Convers.* **2015**, *30*, 784–794. [[CrossRef](#)]
21. Tootoonchian, F. Design and Optimization of a Multi-Turn Variable Reluctance Resolver. *IEEE Sens. J.* **2019**, *19*, 7275–7282. [[CrossRef](#)]
22. Saneie, H.; Nasiri-Gheidari, Z. Generalized Nonoverlapping Tooth Coil Winding Method for Variable Reluctance Resolvers. *IEEE Trans. Ind. Electron.* **2022**, *69*, 5325–5332. [[CrossRef](#)]
23. Bahari, M.; Tootoonchian, F. Performance Analysis of an Outer Rotor Variable Reluctance Resolver. *IEEE Sens. J.* **2022**, *22*, 17761–17768. [[CrossRef](#)]
24. Li, X.; Dai, C.; Chen, W.; Geng, Q.; Wang, H. Position Detection and Speed Recording Method for Power-Off IPMSM in Full-Speed Range Based on Ultrahigh Frequency Signal Injection. *IEEE Trans. Power Electron.* **2023**, *38*, 6918–6922. [[CrossRef](#)]
25. Li, X. Low-Speed Rotating Restart and Speed Recording for Free-Running Sensorless IPMSM Based on Ultrahigh Frequency Sinusoidal Wave Injection. *IEEE Trans. Power Electron.* **2022**, *37*, 15245–15259. [[CrossRef](#)]
26. Li, X.; Jiao, G.; Li, Q.; Chen, W.; Zhang, Z.; Zhang, G. A Position Sensorless Control Strategy for BLDCM Driven by FSTPI Based on Flux-Linkage Function. *World Electr. Veh. J.* **2022**, *13*, 238. [[CrossRef](#)]

**Disclaimer/Publisher’s Note:** The statements, opinions and data contained in all publications are solely those of the individual author(s) and contributor(s) and not of MDPI and/or the editor(s). MDPI and/or the editor(s) disclaim responsibility for any injury to people or property resulting from any ideas, methods, instructions or products referred to in the content.